

# Piezo-phototronic effect boosted catalysis in plasmonic bimetallic ZnO heterostructure with guided fermi level alignment



Y. Zhang <sup>a, b, 1</sup>, S. Wang <sup>a, b, 1</sup>, Y. Zhao <sup>a, b</sup>, Y. Ding <sup>a, b</sup>, Z. Zhang <sup>a, b</sup>, T. Jiang <sup>a, b, c, \*\*\*</sup>, Z.L. Wang <sup>a, b, c, d, \*\*</sup>, L. Li <sup>a, b, c, \*</sup>

<sup>a</sup> School of Resources, Environment and Materials, Center on Nanoenergy Research, School of Physical Science and Technology, Guangxi University, Nanning, 530004, PR China

<sup>b</sup> Beijing Institute of Nanoenergy and Nanosystems, Chinese Academy of Sciences, Beijing, 101400, PR China

<sup>c</sup> University of Chinese Academy of Sciences, Beijing, 100049, PR China

<sup>d</sup> School of Materials Science and Engineering, Georgia Institute of Technology, Atlanta, GA, 30332-0245, USA

## ARTICLE INFO

### Article history:

Received 24 November 2021

Received in revised form

3 January 2022

Accepted 24 January 2022

Available online 31 January 2022

### Keywords:

Piezo-potential

Localized surface plasmon resonance

Piezo-photocatalysis

Nanorod array

## ABSTRACT

High photo-induced carriers (PCs) recombination rate, low PC mobility, and limited solar energy utilization rate are the three main roadblocks that severely limit the photocatalytic activity of semiconductors. In this work, we designed a plasmonic bimetallic ZnO nanorod array (Au/ZnO/Pt) with Au nanoparticles (NPs) located on top of ZnO nanorods and Pt NPs evenly distributed on the ZnO nanorods for improving catalysis through the piezo-phototronic effect. With the rational design of guided Fermi level alignment, the photoinduced hot electrons of Au NPs with localized surface plasmon resonance effect can transfer to Pt NPs through ZnO to promote the separation and migration of PC. More importantly, under the stimulation of ultrasound, ZnO with piezo-phototronic effect generates an interfacial piezo-potential, thereby further promoting the separation and transport of carriers in compliance with the direction of piezo-potential to promote the surface redox reaction. Under the synergy of piezo-phototronic effect and localized surface plasmon resonance effect, the Au/ZnO/Pt realized 97.5% dye degradation in 60 min, which was 1.2, 1.36, and 1.79 folds of that with Au/ZnO/Au, Pt/ZnO/Pt, and ZnO, respectively. The unique plasmonic bimetallic heterostructure with piezo-phototronic effect and guided Fermi level alignment can guide the directional migration of carriers and provides useful instruction for the design of high-efficiency catalysts.

© 2022 Elsevier Ltd. All rights reserved.

## 1. Introduction

With the rapid economic growth, energy and environmental issues have become increasingly prominent. Industrial and sanitary water pollution represents the most serious pollution problem worldwide [1,2]. As a green, energy-saving, and simple method, photocatalysis with semiconductor (SC) photocatalysts has been widely used in water pollution treatment for freshwater availability [3–9]. The artificial photocatalytic process over a SC can be mainly divided into three stages: photoactivation, charge separation and

translocation, and final surface anodic and cathodic redox reactions for degradation of pollutants [10]. In this process, low solar energy utilization rate, low carrier mobility, and high photoinduced electron-hole recombination rate are the three main roadblocks that severely limit the photocatalytic efficiency [11]. Aim at solving these problems, different methods have been developed to improve the catalysis from the aspect of material engineering, including building heterojunction to promote interfacial carrier transportation and separation [12], atom-level modifying or doping to modulate reactive centers [13], constructing ultrathin structure to shorten carrier mobility pathway, and so on [14–16]. However, these methods might narrow the bandgap of the whole catalyst, thus reducing the redox potential of the catalyst to react with pollutants. Therefore, strategies that can simultaneously broaden light utilization and promote carrier separation without reducing the redox potential are more attractive [10,17,18]. For instance, the formation of Schottky junction between plasmonic metal and SC

\* Corresponding author.

\*\* Corresponding author.

\*\*\* Corresponding author.

E-mail addresses: [jiangtao@binn.cas.cn](mailto:jiangtao@binn.cas.cn) (T. Jiang), [zhong.wang@mse.gatech.edu](mailto:zhong.wang@mse.gatech.edu) (Z.L. Wang), [lilinlin@binn.cas.cn](mailto:lilinlin@binn.cas.cn) (L. Li).

<sup>1</sup> Y.Z. and S.W. contributed equally to this work.

with rational Fermi level alignment can not only broaden light utilization but also promote the generation and separation of carriers for finally improving photocatalysis [19–22]. However, it is still far from optimal to realize rapid and efficient water decontamination.

Recently, piezoelectric SCs have brought new blood to traditional photocatalysis with their unique piezo-tronic and piezo-phototronic effect [23]. Piezoelectric nanomaterials, such as wurtzite ZnO and perovskite BaTiO<sub>3</sub> have a relative displacement of the crystal centers of cations and anions under an external mechanical stress, bringing forth dipole polarization and piezo-potential, which can continuously renew the built-in electric field [24]. It can further act as a powerful driving force for modulating the transport and separation of photo-induced carriers (PC) that are generated in the photocatalytic process, thus boosting the catalytic efficiency [25]. For instance, it has been found that the construction of Schottky heterostructures from a plasmonic metal and a piezoelectric SC, such as Au/ZnO, Ag/BaTiO<sub>3</sub>, and Ag/Ag<sub>2</sub>S/BaTiO<sub>3</sub> [26,27] have improved catalytic efficiency under the co-stimulation of the sunlight and a mechanical force. It is due to that under the action of mechanical force to generate the interfacial piezo-potential, the increase of barrier height promoted the separation of carriers and promoted their transport along the direction of piezo-potential [28]. In contrast, the position with decreased barrier height may hinder the separation of carriers [29]. It is inevitable that the piezo-catalyst uniformly supported by the plasma metal strengthens the PC separation at one side of the piezo-potential and weakens the PC separation at the other side. Thus, rational construction of the heterostructures with proper Fermi level alignment, along with its positive corporation with directional piezo-potential, can finally determine the boost of catalysis [22]. For instance, the combination of two metals with different work functions and an SC might guide the directional migration of carriers along with the alignment of the Fermi level [22].

Based on these considerations, herein, we designed a plasmonic bimetallic ZnO heterostructure with a one-dimensional (1D) nanowire array structure (abbr. as AZP) to boost the piezo-photocatalysis. The ZnO nanorods grown on the substrate have uniaxial (C-axis) piezoelectricity, no matter the direction of external mechanical force (Fig. S1, supporting information). The plasmonic Au NPs were located on the top end of the ZnO nanorods and Pt NPs were evenly distributed on the ZnO nanorods. The formation of a pair of Schottky junction of Au/ZnO and Pt/ZnO with Fermi level alignment promoted the separation of carriers under photoexcitation. Moreover, the external ultrasound-triggered piezo-potential of ZnO at the Au/ZnO and Pt/ZnO interfaces acted as the robust promoter to trap electrons and extend the life of carriers. As a result, the catalytic degradation of a model pollutant methyl orange (MO) improved by 45% and 70% relative to mere photocatalysis and mere piezo-catalysis, respectively. In comparison, the bimetallic ZnO heterostructure had a higher catalytic efficiency than the monometallic ones, AZA and PZP. This design proposes an alternative strategy for improving the separation of PC for photocatalysts via the photo-piezotronic effect.

## 2. Results and discussions

The preparation process of the nanocatalysts, including AZA, PZP, and Au/ZnO/Pt (AZP) nanorod arrays, are shown in Fig. 1a. On a fluorine-doped tin oxide (FTO) substrate, a ZnO nanorod array was first grown through a hydrothermal method. Then, Au NPs or Pt NPs were deposited on the vertically grown ZnO nanorods through photoreduction using HAuCl<sub>4</sub> or H<sub>2</sub>PtCl<sub>6</sub> as the metal precursors, respectively. The second round of photoreduction with corresponding noble metal precursors generated AZP, AZA, or PZP

nanorod array. From the scanning electron microscope (SEM) images showing the overhead view and cross-sectional morphology of the ZnO nanorods (Fig. 1b), the nanorods were vertically and closely grown on the FTO glass with a diameter of about 75 nm and length of about 2,000 nm, the large-scale SEM image shows the good uniformity of the ZnO nanorod array (Fig. S3, Supporting Information). Fig. 1c shows the typical SEM image of the AZP nanorod array, in which a lot of small NPs were grown on the surface of the nanorods. From the transmission electron microscope (TEM) and high-resolution TEM images of a single AZP nanorod scraped from the FTO substrate, many small NPs existed and the NPs had different sizes (Fig. 1d and S4, Supporting Information). The lattice fringes of 2.67 Å was assigned to the (002) facets of wurtzite ZnO; those of 2.05 Å and 2.36 Å were assigned to the (111) and (200) facets of cubic Au, respectively, and those of 2.27 Å and 1.96 Å were assigned to the (111) and (200) facets of cubic Pt, respectively (Fig. 1e,f). The Au NPs were mainly distributed on the top end of the ZnO nanorod with a diameter of 15 ± 5 nm, and Pt NPs were uniformly distributed on the whole ZnO nanorod with the smaller size of 4 ± 1 nm. The energy-dispersive x-ray spectroscopy for element mapping also showed a similar trend of element distribution (Fig. 1g, S5c and S6c, Supporting Information). The SEM and TEM images of the monometallic heterostructure AZA and PZP are given in supporting Information (Figs. S2, S5 and S6, Supporting Information). The different sizes of Au and Pt NPs through a similar photoreduction process can be attributed to the different crystallization properties of these two kinds of metal [30].

In the X-ray diffraction patterns of these catalysts, the diffraction peaks of the samples correspond to the wurtzite structured ZnO (JCPDS No. 36-1451) (Fig. S7, Supporting Information). No peaks belonging to other phases including Pt and Au were observed in the several heterostructured samples due to the low content of Pt and Au. X-ray photoelectron spectroscopy was used to detect the elements and their valences (Figs. S8, S9 and S10, Supporting Information). From the high-resolution Zn 2p spectra (Figs. S8b, S9a and S10a, Supporting Information), all the samples of AZP, AZA, and PZP had the two peaks centered at 1,021.5 and 1,044.6 eV, attributed to the existence of Zn 2p<sub>3/2</sub> and Zn 2p<sub>1/2</sub>, respectively. In the high-resolution Au 4f spectra of AZP and AZA (Figs. S8c and S9b, Supporting Information), the two double lines at 83.67 and 87.32 eV were assigned to metal Au 4f<sub>7/2</sub> and Au 4f<sub>5/2</sub>, respectively, corresponding to the binding energies of Au<sup>0</sup>. The double peaks near the Au 4f region at 88.3 and 91.2 eV were assigned to Zn 3p<sub>3/2</sub> and Zn 3p<sub>1/2</sub>, respectively. In the high-resolution Pt 4f spectra for AZP and PZP (Figs. S8d and S10b, Supporting Information), peaks at 70.7/72.13/74.81 eV and 74.05/75.48/78.16 eV were assigned to the metal Pt 4f<sub>7/2</sub> and Pt 4f<sub>5/2</sub>, respectively, associated with binding energies of Pt<sup>0</sup>, Pt<sup>2+</sup>, and Pt<sup>4+</sup>, respectively. The existence of Pt<sup>2+</sup> and Pt<sup>4+</sup> valences was due to the existence of Pt–O bond on the Pt NPs [31]. The oxidation state of Pt usually appears on small Pt NPs due to that the oxygen chemisorption can easily happen at the surface step and kink sites of NPs [32,33]. Interestingly, in the AZP, the peak for low-valence Pt including Pt<sup>0</sup> and Pt<sup>2+</sup> was obvious than that of PZP, which was caused by the accumulation of more electrons on the Pt side. By comparing the peak positions of the binding energy of AZA and PZP (Table S1, Supporting Information), the Au 4f<sub>7/2</sub> and Pt 4f<sub>7/2</sub> peaks in the AZP were nearly unchanged, revealing that the Au and Pt NPs were co-decorated on the ZnO, and no Au–Pt alloy was formed. The piezoelectricity of AZP and ZnO were also confirmed by the voltage response amplitude-voltage curve under a 10 V direct current bias field (Fig. S11, Supporting Information). The piezoelectric coefficient  $d_{33}$  was calculated to be about 80 p.m./V from the slope of the piezo-response amplitude-voltage curve.

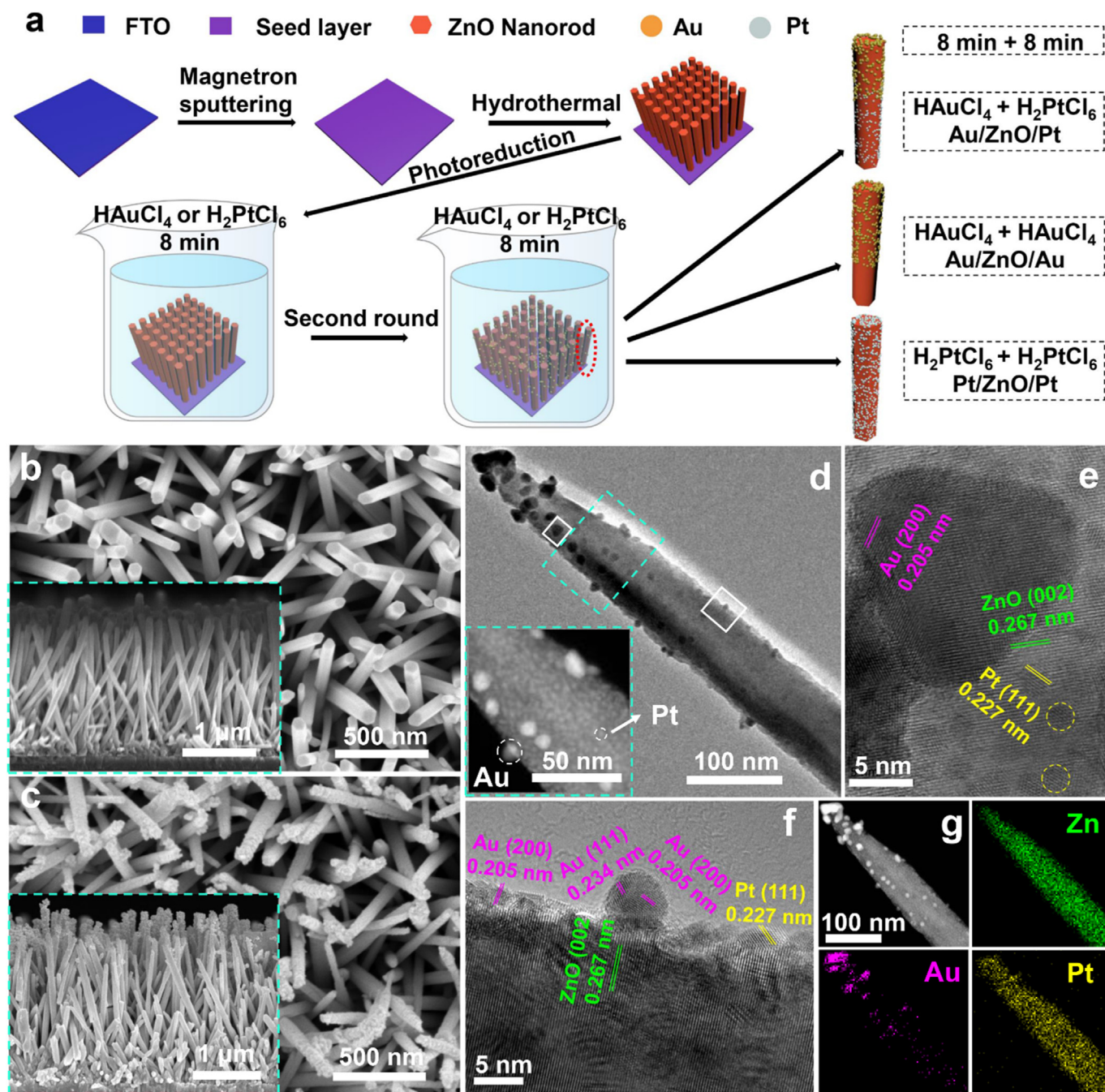


**Fig. 1.** The synthesis process of the nanocatalysts and their structures. (a) The preparation process of the nanocatalysts. SEM images show overhead view of (b) the ZnO and (c) the AZP nanorod array. The insets in (b) and (c) show the corresponding side view. (d) TEM image of the AZP nanorod array with well-defined boundary (inset). (e) and (f) HRTEM images of the AZP nanorod. (g) EDX element mapping of the AZP nanorod. AZP, Au/ZnO/Pt; EDX, energy-dispersive X-ray spectroscopy; HRTEM, high-resolution transmission electron microscope; SEM, scanning electron microscope; TEM, transmission electron microscope.

The photocurrent of the catalysts under full-spectrum light irradiation is shown in Fig. 2a. The photocurrent for all the three kinds of heterostructured nanorod array was improved compared with ZnO. Especially, AZP showed the highest photocurrent density reaching  $141.3 \mu\text{A cm}^{-2}$ , which was about 1.4, 1.56, and two folds of that of AZA, PZP, and ZnO, respectively. Moreover, AZP showed the highest photocurrent stability under the repeated on-off of the light irradiation due to that Pt NPs acted as a promoter to trap electrons and prolong the life of carriers. In comparison, AZA, PZP, and ZnO suffered from decreased photocurrent with the repeated

on-off of the light irradiation. It was worth noting that there was a rising peak of each photocurrent peak when the illuminant was turned on and a peak falling when the illuminant was turned off. It demonstrated that the pyroelectric effect of ZnO contributed to the photocurrent [34]. The pyroelectric current ( $j$ ) can be calculated according to the equations (1)–(3),

$$j = -\partial P_s / \partial t = -(\partial P_s / \partial T)(\partial T / \partial t) \tag{1}$$

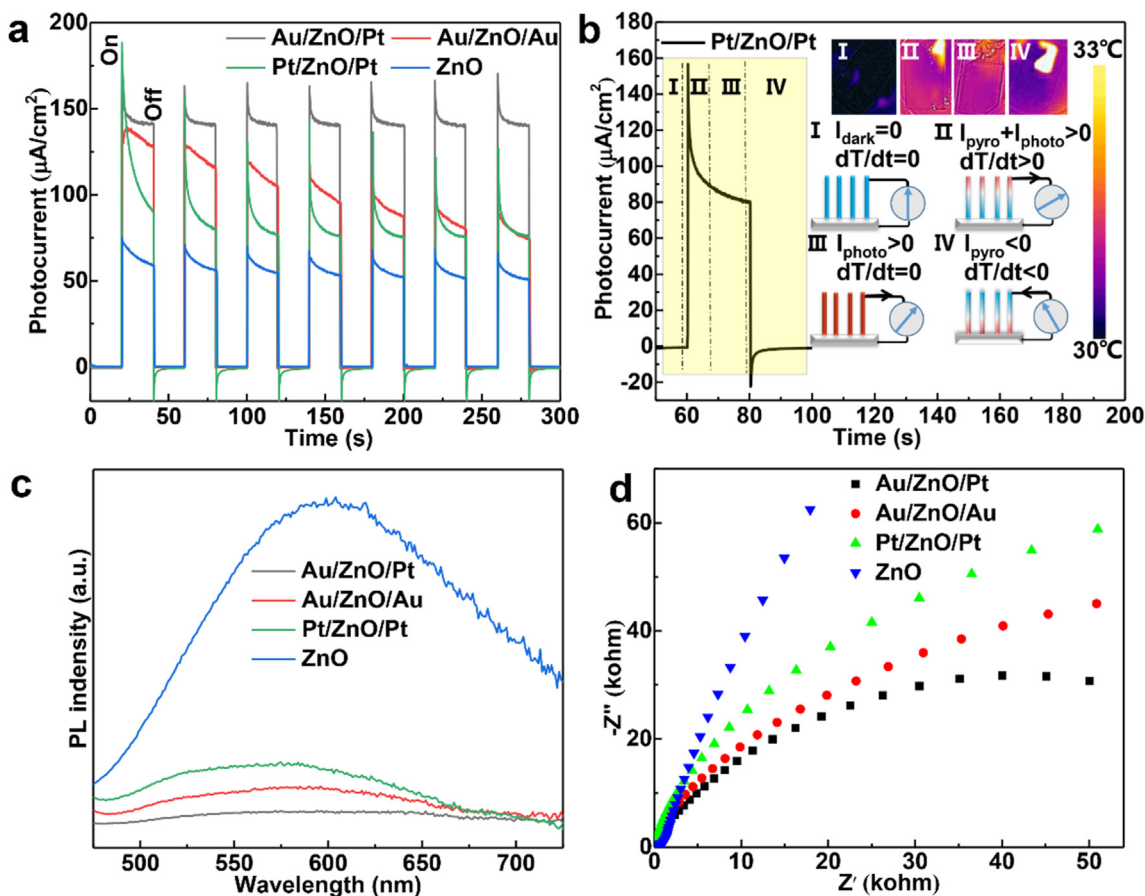


**Fig. 2.** Photoelectrochemical properties of the samples. (a) Time-dependent photocurrent density of the AZP, AZA, PZP, and ZnO nanorod array under full-spectrum light irradiation. (b) Pyroelectric process of PZP with the corresponding inset showing infrared thermal imaging. (c) Photoluminescence spectra and (d) EIS Nyquist plots of ZnO, AZP, AZA, and PZP nanorod array. AZA, Au/ZnO/Au; AZP, Au/ZnO/Pt; EIS, electrochemical impedance spectroscopy; PZP, Pt/ZnO/Pt.

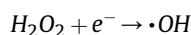
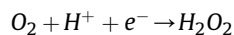
$$\text{let } p = -(\partial P_s / \partial T) \quad (2)$$

$$j = p(\partial T / \partial t) \quad (3)$$

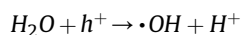
where  $P_s$  is the saturation polarization,  $p$  is the pyroelectric coefficient that is a constant,  $T$  represents the temperature, and  $t$  is the light irradiation time. So,  $j \propto dT/dt$ . From the thermal infrared images in the upper inset of Fig. 2b, the local temperature changed instantaneously (increased from 30 to 31 °C when the light is on and then decreased to 30 °C when the light is off). When the light was turned off (Fig. 2bI), there was no temperature change on the ZnO surface ( $dT/dt = 0$ ), so the pyroelectric current was 0 ( $I_{\text{dark}} = 0$ ). When the light was turned on (Fig. 2bII), the loaded plasmonic metal NPs (Au and Pt) can convert the optical energy of light into local heat and cause the temperature increase ( $dT/dt > 0$ ), so the pyroelectric current appeared ( $I_{\text{pyro}} > 0$ ,  $I_{\text{photo}} > 0$ ) [35]. With the prolonging of the irradiation time (Fig. 2bIII), the local temperature reached a stable level ( $dT/dt = 0$ ), so the pyroelectric current returned to 0 ( $I_{\text{pyro}} = 0$ ,  $I_{\text{photo}} > 0$ ). Then, when the light turned off instantaneously (Fig. 2bIV), ZnO released heat and caused the surface temperature drop ( $dT/dt < 0$ ), so the pyroelectric current decreased to 0 ( $I_{\text{pyro}} < 0$ ,  $I_{\text{photo}} = 0$ ).

As shown in Fig. S12 inset, AZP and AZA showed LSPR shoulder peaks at about 520 nm contributed from Au NPs, whereas there was no observable peak in the visible light region for ZnO and PZP. According to the Tauc plot, the direct bandgaps of AZP, AZA, PZP, and ZnO were calculated to be 3.20, 3.23, 3.20 and 3.24 eV,

respectively. Therefore, the light absorption of the catalysts was mainly confined within the UV region (Fig. S12b, Supporting Information). The Mott–Schottky plot of AZP, AZA, PZP, and ZnO recorded at 1 kHz are presented in Fig. S12 c. The flat band energy of AZP, AZA, PZP, and ZnO are 0.02, 0.02, 0.01, and  $-0.09$  V (vs. Ag/AgCl), respectively. Thus, the calculated  $C_B$  of Au/ZnO/Pt, AZP, AZA, PZP, and ZnO are 0.32, 0.32, 0.31, and 0.21 eV, respectively (the detailed calculation is shown in the Supporting information). The calculated  $V_B$  of AZP, AZA, PZP, and ZnO are 3.52, 3.55, 3.51, and 3.45 eV, respectively. The conduction band level of all the catalysts is more negative than the reduction potential of  $\text{O}_2/\text{H}_2\text{O}_2$  ( $+0.69$  eV), so the following reactions can occur on the conduction band:



The valence band level of all the catalysts is more positive than the reduction potential of  $\text{H}_2\text{O}/\cdot\text{OH}$  ( $+2.38$  eV), so the following reactions can occur on the valence band:



In order to further prove the production of the above reaction, terephthalic acid was used to detect  $\cdot\text{OH}$ , and the fluorescence of the corresponding 2-hydroxyterephthalic acid at 426 nm confirmed the production of  $\cdot\text{OH}$  (Fig. S13a, Supporting

**Information**). The potassium iodide (KI) detection method was used to detect the presence of  $\text{H}_2\text{O}_2$ , and the change in the absorption spectrum of  $\text{I}^{3-}$  at 360 nm confirmed the production of  $\text{H}_2\text{O}_2$  (Fig. S13b, Supporting Information). Therefore, the explanation of the degradation mechanism is shown in Fig. S13c.

The photoluminescence spectroscopy was characterized to study the photocarrier separation ability of the catalysts (Fig. 2c). Under the 325 nm light excitation, AZP had a much lower intensity of the emission peak at about 570 nm relative to the others, revealing the more efficient separation of PC in the AZP heterojunction. This result was consistent with that of the photocurrent stability (Fig. 2a). These results confirmed the highest photoelectric conversion ability of AZP. Electrochemical impedance spectroscopy was used to uncover the carrier transport behavior near the heterojunction region (Fig. 2d). In the Nyquist diagram, the larger the radius of curvature of the arc, the greater the transfer resistance of the interface charge [36]. The AZP heterojunction had the smallest radius of curvature, indicating that it had the lowest PC transfer resistance.

In order to assess the catalytic performance of these nanocatalysts, we used MO as a model dye molecule of wastewater pollutant and detected its degradation under ultrasound (40 kHz, 80 W), full-spectrum light irradiation ( $2 \text{ W cm}^{-2}$ ), and both ultrasound and light irradiation, respectively (Fig. 3). Fig. 3a shows the catalytic activity of different nanocatalysts under ultrasound stimulation. The catalytic activity was defined as  $C/C_0 \times 100\%$  and the corresponding degradation rate was defined as  $(1-C/C_0) \times 100\%$ ,

where  $C_0$  is the MO concentration at  $T = 0$  min when the adsorption equilibrium is reached and  $C$  is the MO concentration after catalysis ( $T = 60$  min). With only the ultrasound-triggered piezoelectric effect for catalysis, the degradation rate for all the nanocatalysts was lower than 30%, indicating that the polarization charges generated by ZnO under the mechanical stress of ultrasonic cavitation had a low catalytic efficiency. Under the full-spectrum light irradiation, degradation of MO was 25% for ZnO, and it increased by about 17–28% for the heterostructured samples, with AZP showing the highest degradation rate of 52% (Fig. 3b). The reason was deduced as follows: The catalytic efficiency of pure ZnO under light stimulation was limited due to the rapid recombination of PC. With the formation of Schottky junction with Au NPs (or Pt NPs), Au NPs (or Pt NPs) caused collective oscillations of the surface electrons under the light excitation, namely local plasma oscillation, which was then converted into hot electrons being injected into ZnO to inhibit the recombination of carriers. As a result, the monometallic PZP and AZA heterostructures had similar degradation efficiency on MO. When the Au NPs and Pt NPs were simultaneously uploaded onto ZnO to form a bimetallic heterostructure, the degradation rate of MO was increased to 52%. Under all-spectrum light irradiation, Au NPs located on the top of ZnO generated collective oscillation of surface electronics to trigger the LSPR effect, which then generated hot electrons. The Pt NPs acted as a co-catalyst to trap electrons, prolonging the life of carriers and further improving the catalytic efficiency. Interestingly, under the co-stimulation of the ultrasound and the all-spectrum light, the degradation rate of MO was greatly

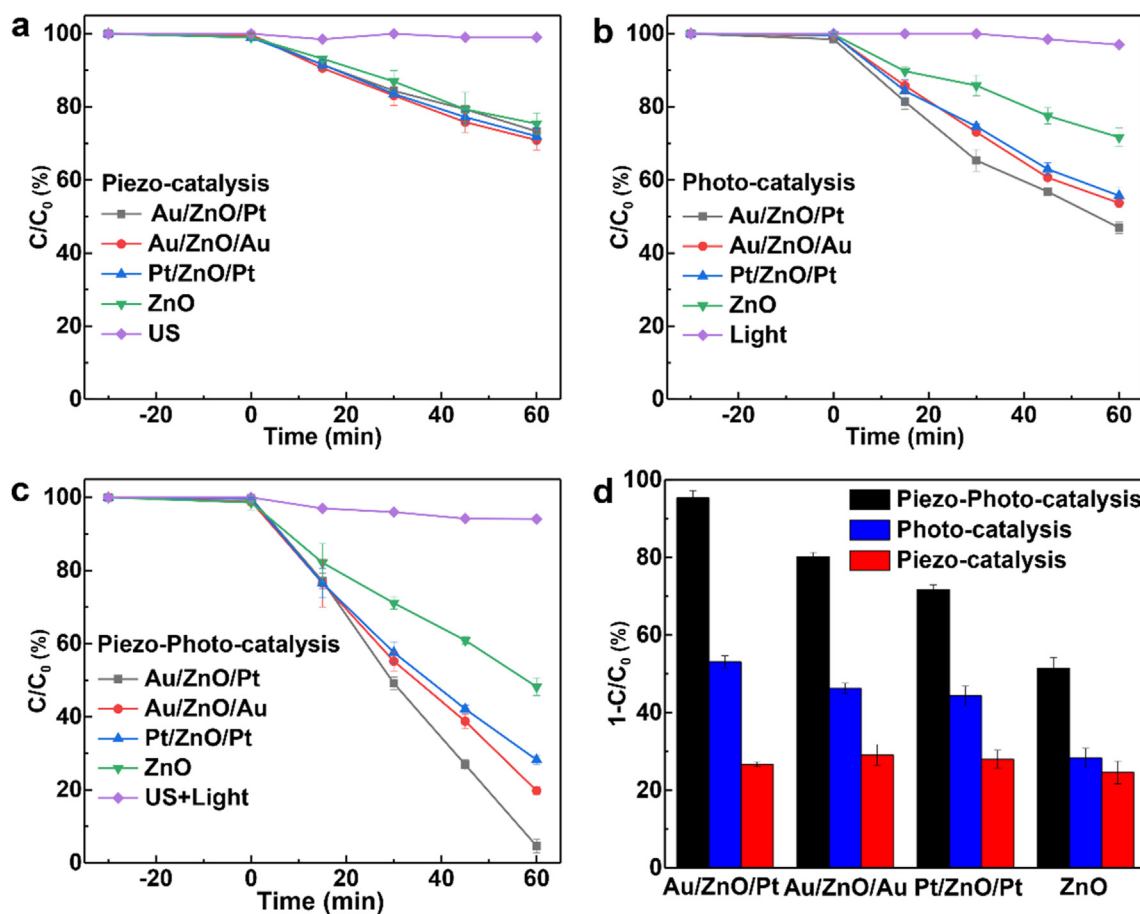


**Fig. 3.** Degradation of MO with AZP, AZA, PZP, and ZnO. (a) Piezo-catalysis under ultrasound. (b) Photocatalysis under full-spectrum light irradiation. (c) Piezo-photocatalysis under both ultrasound and light irradiation. (d) Statistics of the piezo-photocatalysis, photocatalysis, and piezo-catalytic degradation for 60 min with AZP, AZA, PZP, and ZnO. AZA, Au/ZnO/Au; AZP, Au/ZnO/Pt; PZP, Pt/ZnO/Pt.

increased. The degradation rate of MO with AZP, AZA, PZP, and ZnO reached 97.5%, 81%, 72%, and 54%, respectively. Due to the participation of ultrasonic vibration, ZnO can generate a piezoelectric polarization or called built-in electric field along its C-axis. This built-in electric field enhanced the separation and transport of PC at the interface of the Schottky junction by adjusting the bending of the energy band, further increasing the degradation rate (Fig. 3c). The degradation rate of each catalyst under various conditions is shown in Fig. 3d. AZP showed obvious degradation advantages under the synergistic effect of ultrasound and light. Here, the enhancement index of photocatalytic efficiency by piezo-phototronic effect is defined as piezo-photocatalytic efficiency/(piezo-catalytic efficiency+photocatalytic efficiency). The calculated enhancement index of AZP, AZA, PZP, and pure ZnO by piezo-phototronic effect was 1.23, 1.06, 1.02, and 1.13, respectively. After three cycles of catalysis under the co-stimulation of ultrasound and light, the MO degradation efficiency of AZP was 97.5%, 94.4%, and 94.2%, respectively (Fig. S16, Supporting Information). Moreover, the morphology of AZP did not show obvious change after piezo-photocatalysis, indicating its high catalytic stability (Fig. S17, Supporting Information).

To better understand the enhanced catalytic activity of the bimetallic ZnO heterostructure compared with the monometallic ZnO heterostructure and pure ZnO, especially under the co-stimulation of light and ultrasound, the corresponding energy band structure is analyzed (Fig. 4). For photocatalysis under the all-spectrum light, the visible light is mainly absorbed by the metal NPs (Au or Pt), while ZnO with wide bandgap can only absorb the UV light. Due to its limited light absorption and low carrier separation rate, the photocatalytic efficiency of pure ZnO is low [37]. For AZA, Schottky junction is formed between Au NPs and ZnO with the different Fermi levels of Au and ZnO. The Schottky barrier can trap electrons in the  $C_B$  of ZnO to inhibit the recombination of the carriers. Under the light irradiation, the excited hot electrons from plasmonic Au NPs can cross the Schottky barrier and reach the  $C_B$  of

ZnO, leaving the same number of holes on Au to participate in the oxidation degradation of MO. At the same time, the electrons in the  $V_B$  of ZnO transport to its  $C_B$  to form PC (Fig. 4a and S18a). Thus, the photocatalysis of Au/ZnO was improved compared with pure ZnO. However, with the continuous enrichment of electrons in the  $V_B$  of ZnO, the separation of carriers on ZnO will be gradually inhibited. It is the main reason that the photocurrent of AZA decreased with prolonged time as shown in Fig. 2a. Under the external stress from the ultrasonic cavitation, ZnO will generate piezo-potential along the C-axis, which helps to further promote the separation of PC. In addition, the photoinduced electrons and holes are transported along the opposite directions of piezo-potential, promoting the reduction and oxidation reaction, respectively (Fig. 4b) [38]. When Au and Pt NPs are simultaneously loaded onto ZnO to form a bimetallic heterostructure, the charge carriers will redistribute at the interfaces because of the different work function of Au, Pt and ZnO with the sequence of Pt (5.5 eV) > Au (5.1 eV) > ZnO (4.7 eV) [39]. It assists in the diffusion of electrons from ZnO to Au and Pt, forming a pair of Schottky barrier at the contact interfaces of Au/ZnO and Pt/ZnO. The electron can transfer from Au to Pt through ZnO as the Fermi level of Pt is lower than that of Au. For the AZP, under light irradiation, the hot electrons of Au traverse the Schottky barrier and reach the  $C_B$  of ZnO. At the same time, the photoinduced electrons of ZnO transfer from the  $V_B$  to the  $C_B$  and move toward Pt NPs, which act as an electron acceptor to promote the PC separation (Fig. 4c and S18b). The piezo-potential of ZnO under the external stress generates a negative polarization charge at the Au/ZnO interface, causing an upward band bending of ZnO at the interface to promote the separation of PC. It also generates positive polarization charges at the Pt/ZnO interface, causing a downward band bending of ZnO at this interface to promote the photoinduced electrons to migrate to Pt, thereby promoting the separation of the carriers. With the piezo-phototronic effect, the carrier transport is in accordance with the direction of piezo-potential [40], in which the photoinduced electrons are transported along the negative

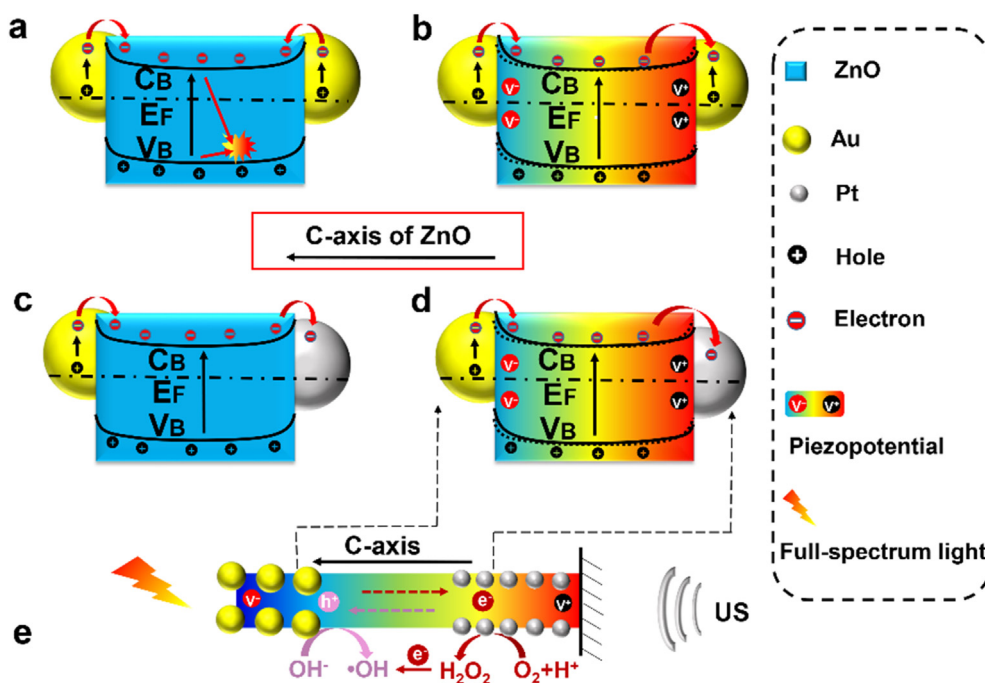


**Fig. 4.** Mechanism for the enhanced catalysis by piezo-phototronic effect and the unique structure under both ultrasound and light irradiation.  $C_B$  and  $V_B$  represent  $C_B$  and  $V_B$  of ZnO, respectively;  $E_F$  represents energy of the Fermi level. (a) AZA under light irradiation. (b) AZA under both ultrasound and light irradiation. (c) AZP under light irradiation. (d) and (e) AZP under both ultrasound and light irradiation. AZA, Au/ZnO/Au; AZP, Au/ZnO/Pt.

direction of the piezo-potential, and the photoinduced holes are transported along the positive direction of the piezo-potential (Fig. 4d and S1) [41] It finally greatly promotes the carrier separation and boost the surface catalytic reaction through the advanced oxidation processes for highly efficient organic pollutant degradation (Fig. 4e).

### 3. Conclusion

In conclusion, the plasmonic bimetallic AZP nanorod array was successfully designed with the guided Fermi level alignment. Importantly, under the ultrasound, ZnO with piezo-phototronic effect can generate piezo-potential at the interface of the Au/ZnO and Pt/ZnO Schottky junctions, inducing the band bending of ZnO at the interfaces with opposite directions to promote the separation of PC along the guided Fermi level alignment. The direction of the promoted carrier transport was in compliance with the direction of piezo-potential. When the ultrasound and light were applied together, the catalytic degradation of model pollutant with AZP increased by 1.2, 1.36, and 1.79 folds relative to AZA, PZP, and ZnO, respectively. The unique 1D bimetallic heterostructure with the piezo-phototronic effect and guided Fermi level alignment has guiding significance for the design of high-efficiency catalysts.

### 4. Experimental section

#### 4.1. Preparation of AZP, AZA, and PZP nanorod array

Au and Pt NPs were deposited in-sequence on ZnO through a photoreduction reaction under irradiation by a UV lamp. For example, for the fabrication of Au/ZnO/Pt, ZnO immersed in  $\text{HAuCl}_4 \cdot 4\text{H}_2\text{O}$  (0.09 mM) was light-irradiated for 8 min to obtain Au/ZnO. Then, the Au/ZnO immersed in  $\text{H}_2\text{PtCl}_6 \cdot 6\text{H}_2\text{O}$  (0.09 mM) was light-irradiated for 8 min to obtain AZP. The other monometallic samples AZA and PZP were prepared following similar procedures. The details about the reagents, synthesis of samples, characterizations, and photoelectrochemical measurements are introduced in the Supplementary file.

#### Data availability

The raw/processed data required to reproduce these findings cannot be shared at this time as the data also forms part of an ongoing study.

#### CRediT authorship contribution statement

Yalong Zhang and Shaobo Wang contributed equally. **Yalong Zhang:** Investigation, Methodology, Data curation, Formal analysis, Writing -original draft. **Shaobo Wang:** Investigation, Methodology, Data curation, Formal analysis. **Yunchao Zhao:** Methodology. **Yiming Ding:** Methodology. **Zeyu Zhang:** Methodology. **Tao Jiang:** Supervision, Writing - review & editing. **Zhong Lin Wang:** Supervision, Resources, Writing - review & editing. **Linlin Li:** Supervision, Conceptualization, Resources, Project administration, Funding acquisition, Writing - review & editing.

#### Declaration of competing interest

The authors declare that they have no known competing financial interests or personal relationships that could have appeared to influence the work reported in this article.

### Acknowledgments

The work was supported by the National Key R&D project from Minister of Science and Technology, China (2016YFA0202703), the National Natural Science Foundation of China (No. 82072065, and 81471784), and the National Youth Talent Support Program.

### Appendix A. Supplementary data

Supplementary data to this article can be found online at <https://doi.org/10.1016/j.mtnano.2022.100177>.

### References

- [1] R.P. Schwarzenbach, B.I. Escher, K. Fenner, T.B. Hofstetter, C.A. Johnson, U.v. Gunten, B. Wehrli, The challenge of micropollutants in aquatic systems, *Science* 313 (2006) 1072–1077.
- [2] M.S. Mauter, I. Zucker, F. Perreault, J.R. Werber, J.-H. Kim, M. Elimelech, The role of nanotechnology in tackling global water challenges, *Nat. Sustain.* 1 (2018) 166–175.
- [3] A. Fujishima, K. Honda, Electrochemical photolysis of water at a semiconductor electrode, *Nature* 238 (1972) 37–38.
- [4] C.V. Reddy, I.N. Reddy, R. Koutavarapu, K.R. Reddy, T.A. Saleh, T.M. Aminabhavi, J. Shim, Novel edge-capped  $\text{ZrO}_2$  nanoparticles onto  $\text{V}_2\text{O}_5$  nanowires for efficient photosensitized reduction of chromium (Cr (VI)), photoelectrochemical solar water splitting, and electrochemical energy storage applications, *Chem. Eng. J.* 430 (2022) 132988.
- [5] R. Koutavarapu, M.R. Tamtam, S.-G. Lee, M.C. Rao, D.-Y. Lee, J. Shim, Synthesis of 2D  $\text{NiFe}_2\text{O}_4$  nanoplates/2D  $\text{Bi}_2\text{WO}_6$  nanoflakes heterostructure: an enhanced Z-scheme charge transfer and separation for visible-light-driven photocatalytic degradation of toxic pollutants, *J. Environ. Chem. Eng.* 9 (2021) 105893.
- [6] R. Koutavarapu, K. Syed, S. Pagidi, M.Y. Jeon, M.C. Rao, D.-Y. Lee, J. Shim, An effective  $\text{CuO}/\text{Bi}_2\text{WO}_6$  heterostructured photocatalyst: analyzing a charge-transfer mechanism for the enhanced visible-light-driven photocatalytic degradation of tetracycline and organic pollutants, *Chemosphere* 287 (2022) 132015.
- [7] R. Koutavarapu, C.V. Reddy, K. Syed, K.R. Reddy, T.A. Saleh, D.-Y. Lee, J. Shim, T.M. Aminabhavi, Novel Z-scheme binary zinc tungsten oxide/nickel ferrite nanohybrids for photocatalytic reduction of chromium (Cr (VI)), photoelectrochemical water splitting and degradation of toxic organic pollutants, *J. Hazard Mater.* 423 (2022) 127044.
- [8] M. Mousavi, A. Habibi-Yangjeh, M. Abitorabi, Fabrication of novel magnetically separable nanocomposites using graphitic carbon nitride, silver phosphate and silver chloride and their applications in photocatalytic removal of different pollutants using visible-light irradiation, *J. Colloid Interface Sci.* 480 (2016) 218–231.
- [9] S.J. Lee, H.J. Jung, R. Koutavarapu, S.H. Lee, M. Arumugam, J.H. Kim, M.Y. Choi, ZnO supported Au/Pd bimetallic nanocomposites for plasmon improved photocatalytic activity for methylene blue degradation under visible light irradiation, *Appl. Surf. Sci.* 496 (2019) 143665.
- [10] X. Xue, W. Zang, P. Deng, Q. Wang, L. Xing, Y. Zhang, Z.L. Wang, Piezo-potential enhanced photocatalytic degradation of organic dye using ZnO nanowires, *Nano Energy* 13 (2015) 414–422.
- [11] S. Tu, Y. Guo, Y. Zhang, C. Hu, T. Zhang, T. Ma, H. Huang, Piezocatalysis and piezo-photocatalysis: catalysts classification and modification strategy, reaction mechanism, and practical application, *Adv. Funct. Mater.* 30 (2020) 2005158.
- [12] Q. Xu, L. Zhang, B. Cheng, J. Fan, J. Yu, S-scheme heterojunction photocatalyst, *Inside Chem.* 6 (2020) 1543–1559.
- [13] H. Huang, S. Tu, C. Zeng, T. Zhang, A.H. Reshak, Y. Zhang, Macroscopic polarization enhancement promoting photo- and piezoelectric-induced charge separation and molecular oxygen activation, *Angew. Chem. Int. Ed.* 56 (2017) 11860–11864.
- [14] F. Chen, T. Ma, T. Zhang, Y. Zhang, H. Huang, Atomic-level charge separation strategies in semiconductor-based photocatalysts, *Adv. Mater.* 33 (2021) 2005256.
- [15] J. Hu, L. Yu, J. Deng, Y. Wang, K. Cheng, C. Ma, Q. Zhang, W. Wen, S. Yu, Y. Pan, J. Yang, H. Ma, F. Qi, Y. Wang, Y. Zheng, M. Chen, R. Huang, S. Zhang, Z. Zhao, J. Mao, X. Meng, Q. Ji, G. Hou, X. Han, X. Bao, Y. Wang, D. Deng, Sulfur vacancy-rich  $\text{MoS}_2$  as a catalyst for the hydrogenation of  $\text{CO}_2$  to methanol, *Nat. Catal.* 4 (2021) 242–250.
- [16] Y. Chen, L. Su, M. Jiang, X. Fang, Switch type PANI/ZnO core-shell microwire heterojunction for UV photodetection, *J. Mater. Sci. Technol.* 105 (2022) 259–265.
- [17] H. Guan, G. Mao, T. Zhong, T. Zhao, S. Liang, L. Xing, X. Xue, A self-powered UV photodetector based on the hydrovoltaic and photoelectric coupling properties of ZnO nanowire arrays, *J. Alloys Compd.* 867 (2021) 159073.
- [18] Z. Wang, T. Hu, H. He, Y. Fu, X. Zhang, J. Sun, L. Xing, B. Liu, Y. Zhang, X. Xue, Enhanced  $\text{H}_2$  production of  $\text{TiO}_2/\text{ZnO}$  nanowires Co-using solar and

- mechanical energy through piezo-photocatalytic effect, *ACS Sustain. Chem. Eng.* 6 (2018) 10162–10172.
- [19] Z. Liu, W. Hou, P. Pavaskar, M. Aykol, S.B. Cronin, Plasmon resonant enhancement of photocatalytic water splitting under visible illumination, *Nano Lett.* 11 (2011) 1111–1116.
- [20] S. Mubeen, G. Hernandez-Sosa, D. Moses, J. Lee, M. Moskovits, Plasmonic photosensitization of a wide band gap semiconductor: converting plasmons to charge carriers, *Nano Lett.* 11 (2011) 5548–5552.
- [21] A. Tanaka, S. Sakaguchi, K. Hashimoto, H. Kominami, Preparation of Au/TiO<sub>2</sub> with metal cocatalysts exhibiting strong surface plasmon resonance effective for photoinduced hydrogen formation under irradiation of visible light, *ACS Catal.* 3 (2013) 79–85.
- [22] A. Tanaka, K. Nakanishi, R. Hamada, K. Hashimoto, H. Kominami, Simultaneous and stoichiometric water oxidation and Cr(VI) reduction in aqueous suspensions of functionalized plasmonic photocatalyst Au/TiO<sub>2</sub>–Pt under irradiation of green light, *ACS Catal.* 3 (2013) 1886–1891.
- [23] W. Wu, C. Pan, Y. Zhang, X. Wen, Z.L. Wang, Piezotronics and piezo-phototronics – from single nanodevices to array of devices and then to integrated functional system, *Nano Today* 8 (2013) 619–642.
- [24] Z.L. Wang, Piezotronic and piezophototronic effects, *J. Phys. Chem. Lett.* 1 (2010) 1388–1393.
- [25] Z. Liu, X. Yu, L. Li, Piezopotential augmented photo- and photoelectro-catalysis with a built-in electric field, *Chin. J. Catal.* 41 (2020) 534–549.
- [26] S. Xu, L. Guo, Q. Sun, Z.L. Wang, Piezotronic effect enhanced plasmonic photocatalysis by AuNPs/BaTiO<sub>3</sub> heterostructures, *Adv. Funct. Mater.* 29 (2019) 1808737.
- [27] Y. Lei, S. Xu, M. Ding, L. Li, Q. Sun, Z.L. Wang, Enhanced photocatalysis by synergistic piezotronic effect and exciton–plasmon interaction based on (Ag-Ag<sub>2</sub>S)/BaTiO<sub>3</sub> heterostructures, *Adv. Funct. Mater.* 30 (2020) 2005716.
- [28] L. Pan, S. Sun, Y. Chen, P. Wang, J. Wang, X. Zhang, J.-J. Zou, Z.L. Wang, Advances in piezo-phototronic effect enhanced photocatalysis and photoelectrocatalysis, *Adv. Energy Mater.* 10 (2020) 2000214.
- [29] W. Wu, Z.L. Wang, Piezotronics and piezo-phototronics for adaptive electronics and optoelectronics, *Nat. Rev. Mater.* 1 (2016) 16031.
- [30] L.K. Ono, B. Yuan, H. Heinrich, B.R. Cuenya, Formation and thermal stability of platinum oxides on size-selected platinum nanoparticles: Support effects, *J. Phys. Chem. C* 114 (2010) 22119–22133.
- [31] Z. Zhang, A. Li, S.-W. Cao, M. Bosman, S. Li, C. Xue, Direct evidence of plasmon enhancement on photocatalytic hydrogen generation over Au/Pt-decorated TiO<sub>2</sub> nanofibers, *Nanoscale* 6 (2014) 5217–5222.
- [32] A.S. Aricò, A.K. Shukla, H. Kim, S. Park, M. Min, V. Antonucci, An XPS study on oxidation states of Pt and its alloys with Co and Cr and its relevance to electroreduction of oxygen, *Appl. Surf. Sci.* 172 (2001) 33–40.
- [33] Y. Ding, Y. Wang, L. Zhang, H. Zhang, C.M. Li, Y. Lei, Preparation of TiO<sub>2</sub>–Pt hybrid nanofibers and their application for sensitive hydrazine detection, *Nanoscale* 3 (2011) 1149–1157.
- [34] D. Xiang, Z. Liu, M. Wu, H. Liu, X. Zhang, Z. Wang, Z.L. Wang, L. Li, Enhanced piezo-photoelectric catalysis with oriented carrier migration in asymmetric Au–ZnO nanorod array, *Small* 16 (2020) 1907603.
- [35] Z. Wang, R. Yu, C. Pan, Z. Li, J. Yang, F. Yi, Z.L. Wang, Light-induced pyroelectric effect as an effective approach for ultrafast ultraviolet nanosensing, *Nat. Commun.* 6 (2015) 8401.
- [36] Z. Liu, L. Wang, X. Yu, J. Zhang, R. Yang, X. Zhang, Y. Ji, M. Wu, L. Deng, L. Li, Z.L. Wang, Piezoelectric-effect-enhanced full-spectrum photoelectrocatalysis in p–n heterojunction, *Adv. Funct. Mater.* 29 (2019) 1807279.
- [37] Z. Liang, C.-F. Yan, S. Rtimi, J. Bandara, Piezoelectric materials for catalytic/photocatalytic removal of pollutants: recent advances and outlook, *Appl. Catal. B Environ.* 241 (2019) 256–269.
- [38] H. Li, Y. Sang, S. Chang, X. Huang, Y. Zhang, R. Yang, H. Jiang, H. Liu, Z.L. Wang, Enhanced ferroelectric-nanocrystal-based hybrid photocatalysis by ultrasonic-wave-generated piezophototronic effect, *Nano Lett.* 15 (2015) 2372–2379.
- [39] Q. Liu, Z. Wang, H. Chen, H.-Y. Wang, H. Song, J. Ye, Y. Weng, Rules for selecting metal cocatalyst based on charge transfer and separation efficiency between ZnO nanoparticles and noble metal cocatalyst Ag/Au/Pt, *Chem-CatChem* 12 (2020) 3838–3842.
- [40] L. Wang, S. Liu, Z. Wang, Y. Zhou, Y. Qin, Z.L. Wang, Piezotronic effect enhanced photocatalysis in strained anisotropic ZnO/TiO<sub>2</sub> nanoplatelets via thermal stress, *ACS Nano* 10 (2016) 2636–2643.
- [41] L. Zhu, Z.L. Wang, Recent progress in piezo-phototronic effect enhanced solar cells, *Adv. Funct. Mater.* 29 (2019) 1808214.